

Various facets of magnetic charge correlation: Micromagnetic and distorted-wave Born approximation simulations study

G. Yumnam , J. Guo , and D. K. Singh**Department of Physics and Astronomy, University of Missouri, Columbia, Missouri 65211, USA*

(Received 18 May 2021; revised 12 October 2021; accepted 12 October 2021; published 25 October 2021)

The emergent concept of the magnetic charge quasiparticle provides a new realm to study the evolution of magnetic properties in two-dimensional artificially frustrated magnets. We report on the exploration of magnetic phases due to various magnetic charge correlation using the complementary numerical techniques of micromagnetic and distorted-wave Born approximation simulations in artificial permalloy honeycomb lattice. The honeycomb element length varies between 10 nm and 100 nm, while the width and thickness are kept within the single domain limit. In addition to the charge ordered loop state, we observe disordered charge arrangement, characterized by the random distribution of $\pm Q$ charges, in single domain size honeycomb lattice. As the length of the honeycomb element increases, low multiplicity magnetic charges tend to form contiguous bands in thinner lattice. Thin honeycomb lattice with 100 nm element length exhibits a perfect spin ice pattern, which remains unaffected by the modest increase in the width of element size. We simulate scattering profiles under the pretext of distorted-wave Born approximation formalism for the micromagnetic phases. The results are expected to provide useful guidance in the experimental investigation of magnetic phases in an artificial honeycomb magnet.

DOI: [10.1103/PhysRevB.104.134429](https://doi.org/10.1103/PhysRevB.104.134429)

I. INTRODUCTION

The honeycomb lattice structure has generated significant research interest in recent times—primarily motivated by the unusual electronic and magnetic properties, as found in graphene and nanostructured magnetic honeycomb lattice, respectively [1–3]. Artificial magnetic honeycomb lattice is a prominent research venue to explore novel magnetism in reduced dimensionality. Originally conceived to explore the magnetic analog of ice rule and associated Dirac’s effective monopoles using standard experimental techniques [4], such as magnetic force microscopy and the x-ray dichroism method, it has become a subject of extensive investigation to find new properties of geometrically frustrated magnets [2]. In recent years, artificially created magnetic honeycomb lattice is demonstrated to exhibit a broad and tunable range of novel magnetic phenomena that are difficult to achieve in a naturally occurring magnet, such as the entropy-driven magnetic charge-ordered state due to the spin chirality [1,5]. At low enough temperature, the magnetic correlation develops into a long range ordered spin solid state density, which is manifested by the periodic arrangement of the vortex loops of opposite chirality across the lattice [6,7]. One of the underlying assumptions in the theoretical analysis of magnetic properties in two-dimensional honeycomb lattice is based on the proposition that a magnetic moment can be considered as a pair of magnetic charges of opposite polarities, as if it is a “dumbbell,” that interact via the magnetic Coulomb interaction [4,8,9]. Consequently, honeycomb vertices are occupied by two types of magnetic charges: ± 3 and ± 1 units that are associated with the peculiar moment configurations

where the magnetic moment, aligned along the length of the element due to the shape anisotropy, either points to or away from the vertex at the same time or two of them point to (or away) from the vertex and one points away (or to) from the vertex, respectively [10]. These moment arrangements are also called “all in or all out” and “two in and one out” (or vice versa) spin configurations.

Magnetic charges are represented by the Pauli matrices quantum operator [5]. The quantum mechanical properties of magnetic charge, also termed as quasi particle [1], enable the exploration of dynamic magnetic states in artificial Kagome ice [11–13]. One of such states is the quantum disordered magnetic ground state due to the competing energetics between the nearest neighbor and the next nearest neighbor exchange interactions (J_1 and J_2 , respectively) [14,15]. However, the thermal tunability of lattice magnetization is necessary to the realization of such a novel state, as it facilitates magnetic charge dynamics to incite a massively degenerate ground state at $T \rightarrow 0$ K [16]. Experimental evidence to this proposition was recently obtained in a magnetic honeycomb lattice with thermally tunable characteristic, made of single domain size connecting elements [17]. Besides the emergent magnetic properties, magnetic charge quasiparticles are also found to develop the magnetic analog of a quintessential electronic state of the Wigner crystal in the simultaneous applications of electric current and magnetic field [18]. Magnetic charge’s versatility in the manifestation of various ground state properties under different thermal, electrical, and magnetic field tuning conditions have spurred a plethora of new research. In this article, we report a systematic study of the evolution of magnetic charge correlation as a function of the geometrical tuning parameter, e.g., variation in element size in artificial permalloy honeycomb lattice. The honeycomb element length varies between 10 nm and

*singhdk@missouri.edu

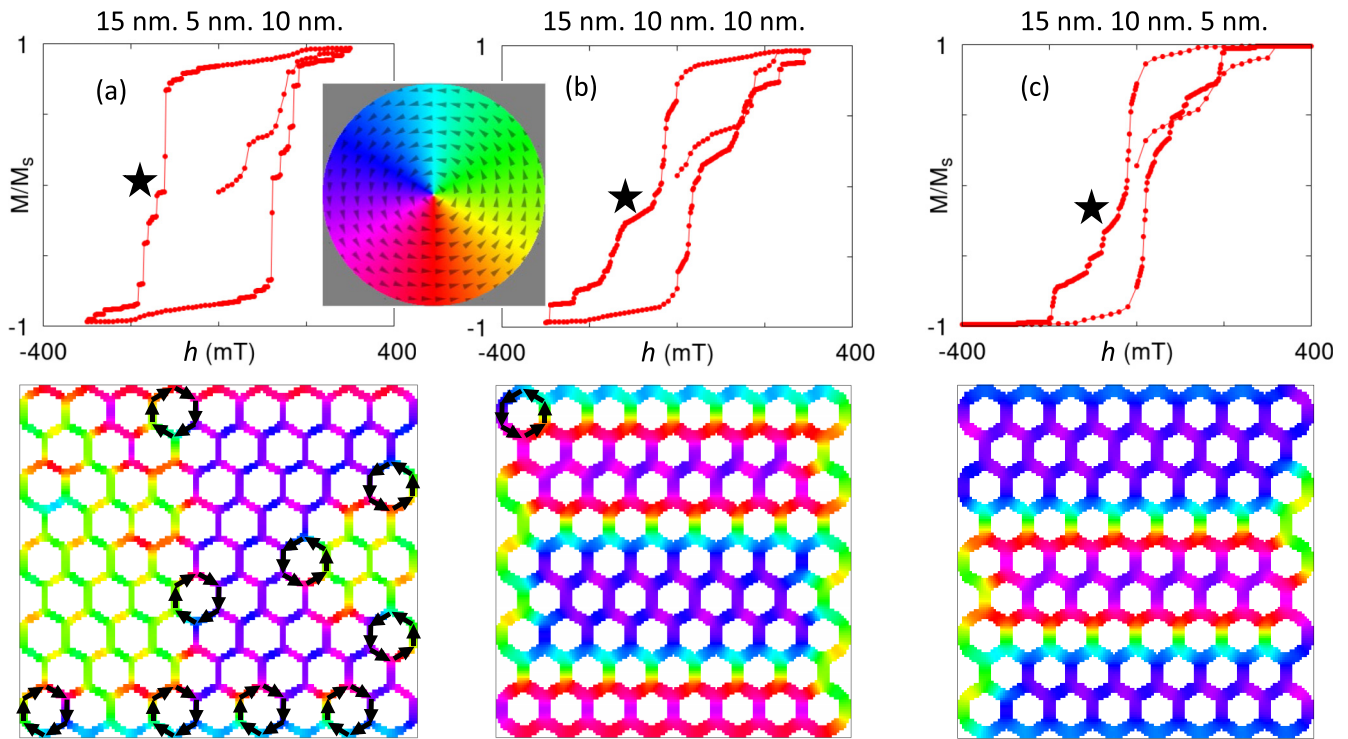


FIG. 1. Micromagnetic simulation of permalloy honeycomb lattice, made of single domain element size. Top panel—magnetic hysteresis loop generated by MM simulation for various element size honeycombs. Bottom panel—magnetic charge configuration after magnetic transition near zero magnetic field (marked by asterisk). (a) Element size of $15 \text{ nm} \times 5 \text{ nm} \times 10 \text{ nm}$. The system tends to develop the spin solid loop state in thin honeycomb lattice. Inset shows the color profile of magnetization direction. (b) Element size of $15 \text{ nm} \times 10 \text{ nm} \times 10 \text{ nm}$. As the lattice elements become broader, disordered configuration of magnetic charges arise. (c) Element sizes of $15 \text{ nm} \times 10 \text{ nm} \times 5 \text{ nm}$. Spin ice state is prominent in this case.

100 nm, while the width and the thickness vary between the two limits of 5 nm and 10 nm. Since width and thickness dimensions are always smaller than the typical domain size in permalloy, $\sim 18 \text{ nm}$ [19], the honeycomb elements in this study are either single domain or constricted single domain in at least two directions. Micromagnetic simulations reveal that 5 nm thick honeycomb with 100 nm long elements develops a perfect spin ice state. As the element size decreases, the system exhibits a variety of interesting charge configurations that include the charge ordered loop state, extending to the spin solid state, disordered phase, and a stripelike contiguous band of $\pm Q$ charges in a 50 nm element size lattice. The micromagnetic simulation study is complemented by the detailed modeling of scattering profiles using the distorted-wave Born approximation (DWBA) formalism for the theoretically generated magnetic phases. The DWBA profiles can act as a guide in the experimental investigation of theoretical phases using macroscopic probes, such as neutron reflectometry.

There are several experimental methods to determine the nature of magnetic charge correlations or infer about the phase transition process in two-dimensional artificial spin ice. Some of the notable techniques include magnetic force microscopy, x-ray dichroism method, nonlinear susceptibility analysis, photoemission electron microscopy, and polarized neutron reflectometry (PNR) [2,6,7,12,20]. While some of these techniques are suitable for elucidating the local

magnetic correlation, statistical probes, such as the PNR method, are by design the bulk experimental procedure to deduce both the short range and the long range nature of correlations [21]. For instance, the spin solid state manifests the long range ordered arrangement of magnetic charges. Therefore, it is desirable to probe such a characteristic in a sample consisting of the macroscopic ensemble of honeycomb lattice units using a scattering method, such as the PNR measurement technique. However, unlike magnetic force microscopy, neutron reflectometry measurement does not yield direct information regarding the magnetic correlation in real space. It is typically inferred from the modeling of the off-specular reflectometry profile using the established numerical approach of the distorted-wave Born approximation (DWBA) formalism [6,22]. Numerical modeling using the DWBA method is nontrivial. In this article, we present DWBA simulations of various charge correlated phases, as predicted by theoretical calculations [1] and micromagnetic simulations, in artificial magnetic (permalloy, $\text{Ni}_{0.8}\text{Fe}_{0.2}$) honeycomb lattice systems of varying element sizes. Here is the outline of the article: first, we describe the micromagnetic (MM) simulations in low temperature limit $T \rightarrow 0 \text{ K}$ regarding the magnetic charge correlation on honeycomb vertices of varying element sizes. Second, DWBA simulated reflectometry profiles for various charge correlations are depicted using the contour maps in reciprocal space. For this purpose, some of the relevant

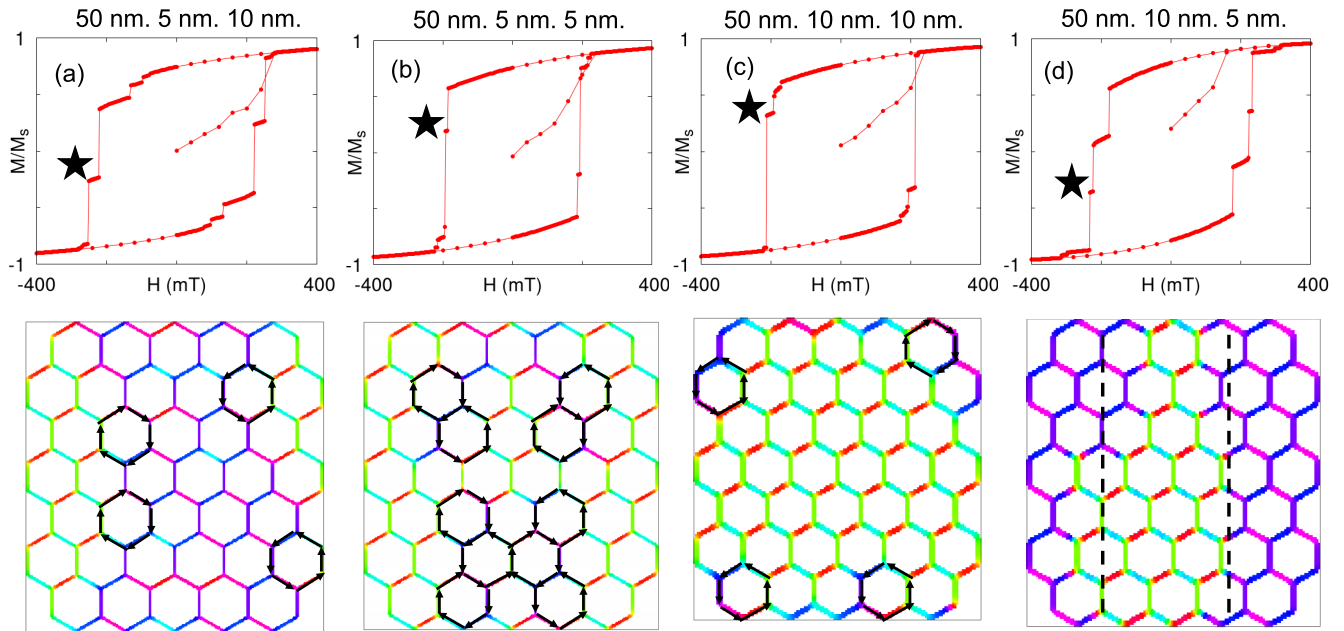


FIG. 2. MM simulation of permalloy honeycomb lattice with 50 nm element length. Top panel—magnetic hysteresis loop generated. Bottom panel—magnetic charge configuration after magnetic transition (marked by asterisk). (a) Element size of 50 nm × 5 nm × 10 nm. The system tends to develop the spin solid loop state as $T \rightarrow 0$ K. (b) Element size of 50 nm × 5 nm × 5 nm. As the thickness of the honeycomb lattice decreases, more loops are formed and tend to be close to each other and the system tends to develop a complete spin solid loop state. (c) Element sizes of 50 nm × 10 nm × 10 nm. As the lattice becomes wider, the system tends to develop spin ice state as $T \rightarrow 0$ K. (d) Element sizes of 50 nm × 10 nm × 5 nm. Contiguous bands of $\pm Q$ magnetic charges, reminiscent of stripe-type order, develop in thin honeycomb lattice with wider element.

parameters from the recently reported experimental results are utilized [6,10,17]. Finally, we summarize the results with a brief outlook for the future research.

II. MICROMAGNETIC SIMULATIONS

Micromagnetic simulations are carried out using the Object Oriented MicroMagnetic Framework (OOMMF) [23]. Mag-

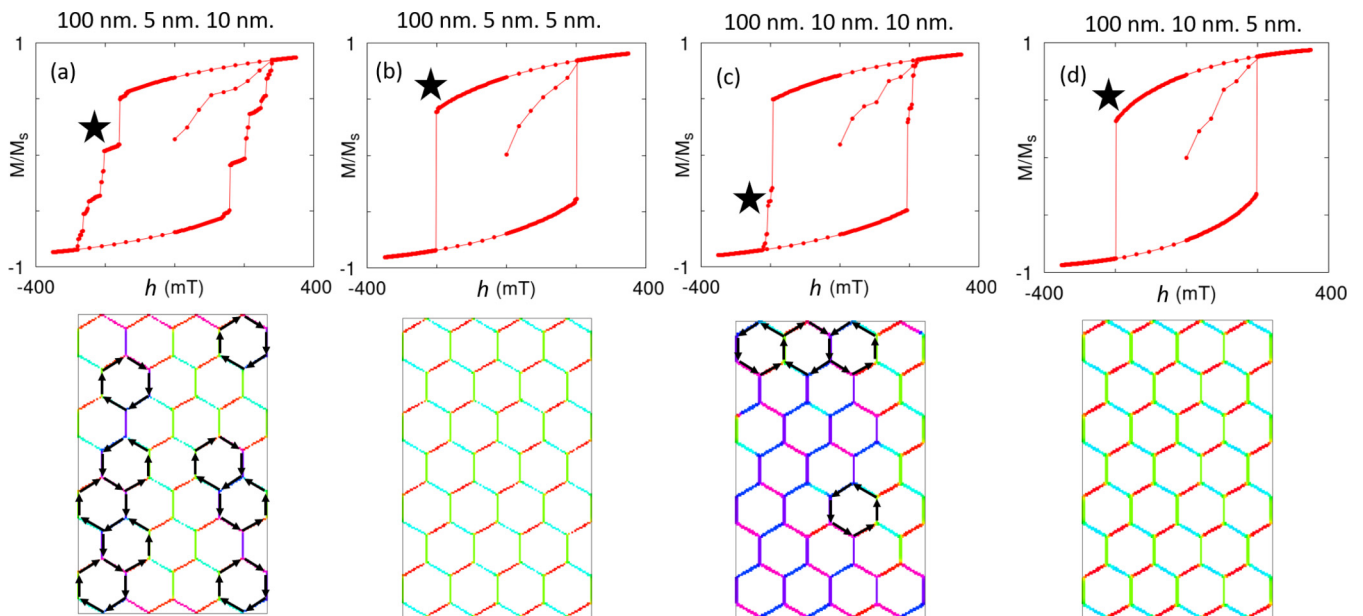


FIG. 3. MM simulation of 100 nm element length. (a) Element size of 100 nm × 5 nm × 10 nm. The system tends to develop the spin solid loop state as $T \rightarrow 0$ K. (b) Element size of 100 nm × 5 nm × 5 nm. Magnetic phase near zero field is primarily dominated by the spin ice-type magnetic charge configuration. (c) Element size of 100 nm × 10 nm × 10 nm. As the lattice becomes wider, fewer loops are founded. (d) Element size of 100 nm × 10 nm × 5 nm. Near zero field, the magnetic phase in thin honeycomb lattice with wider elements is also primarily dominated by the spin ice-type magnetic charge configuration.

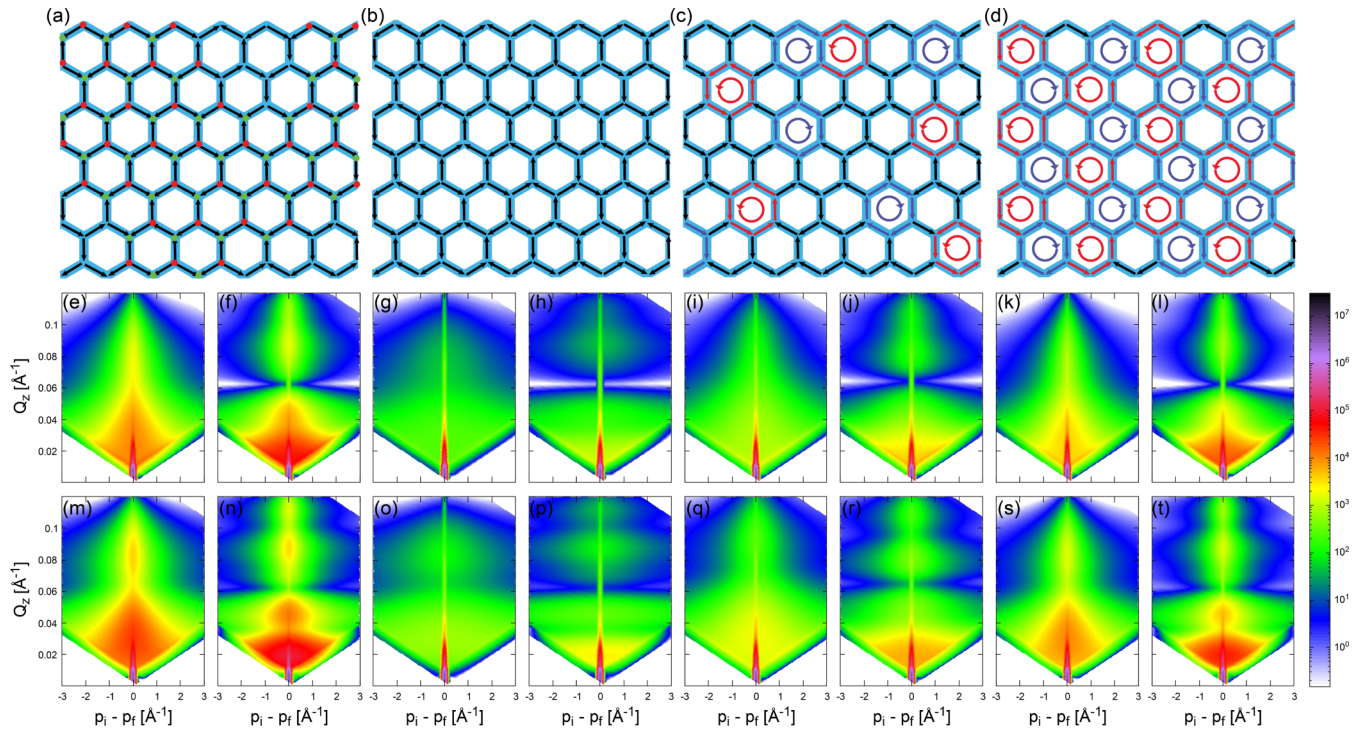


FIG. 4. DWBA simulation of permalloy honeycomb lattice of 12 nm element length. (a)–(d) Top panel—magnetic charge configurations of disordered, spin ice, magnetic charge ordered, and spin solid loop states. (e),(f),(m),(n) DWBA simulation of disordered magnetic charge configuration [shown in (a)] in various element size lattices of $12 \text{ nm} \times 5 \text{ nm} \times 5 \text{ nm}$, $12 \text{ nm} \times 5 \text{ nm} \times 10 \text{ nm}$, $12 \text{ nm} \times 10 \text{ nm} \times 5 \text{ nm}$, and $12 \text{ nm} \times 10 \text{ nm} \times 10 \text{ nm}$, respectively. (g),(h),(o),(p) DWBA simulation of spin ice configuration [shown in (b)] in various element size lattices of $12 \text{ nm} \times 5 \text{ nm} \times 5 \text{ nm}$, $12 \text{ nm} \times 5 \text{ nm} \times 10 \text{ nm}$, $12 \text{ nm} \times 10 \text{ nm} \times 5 \text{ nm}$, and $12 \text{ nm} \times 10 \text{ nm} \times 10 \text{ nm}$, respectively. (i),(j),(q),(r) DWBA simulation of magnetic charge ordered state [shown in (c)] in various element size lattices of $12 \text{ nm} \times 5 \text{ nm} \times 5 \text{ nm}$, $12 \text{ nm} \times 5 \text{ nm} \times 10 \text{ nm}$, $12 \text{ nm} \times 10 \text{ nm} \times 5 \text{ nm}$, and $12 \text{ nm} \times 10 \text{ nm} \times 10 \text{ nm}$, respectively. (k),(l),(s),(t) DWBA simulation of spin solid state [shown in (d)] in various element size lattices of $12 \text{ nm} \times 5 \text{ nm} \times 5 \text{ nm}$, $12 \text{ nm} \times 5 \text{ nm} \times 10 \text{ nm}$, $12 \text{ nm} \times 10 \text{ nm} \times 5 \text{ nm}$, and $12 \text{ nm} \times 10 \text{ nm} \times 10 \text{ nm}$, respectively

netic field dependent magnetization evolution, together with the flexible geometry specification, allows us to study the response of the magnetization as a function of magnetic field, applied in plane to the honeycomb thin film. The simulated geometry is made of a honeycomb lattice with connected topography where the permalloy ($\text{Ni}_{0.8}\text{Fe}_{0.2}$) element length varies between 10 nm and 100 nm. For MM simulations, honeycomb lattices are discretized into grids with the individual mesh size of $2 \times 2 \times 1.25 \text{ nm}^3$ (X , Y , and Z) and $2 \times 2 \times 2.5 \text{ nm}^3$ for thicknesses 5 nm and 10 nm, respectively. Nanostructured magnetic materials were previously simulated with similar grid and mesh sizes [24] The simulation utilizes the Landau-Lifshitz-Gilbert equation of magnetization relaxation in a damped medium. It is given by [25–27]

$$\frac{d\mathbf{m}}{dt} = -\gamma \mathbf{m} \times \mathbf{h}_{eff} + \alpha \mathbf{m} \times \frac{d\mathbf{m}}{dt}, \quad (1)$$

where γ is the gyromagnetic ratio and α is the damping constant. The effective field is given by $\mathbf{h}_{eff}(T=0) = -\delta \mathbf{H} / \delta \mathbf{m}$. The Hamiltonian, \mathbf{H} , of the system consists of four terms: exchange energy, uniaxial anisotropic energy, magnetostatic energy, and the Zeeman energy. For MM simulations, we have used the typical values for permalloy material, e.g., exchange stiffness $A = 1.0 \times 10^{-11} \text{ J/m}$, saturation magnetization $M_s = 1.0 \times 10^6 \text{ A/m}$, uniaxial anisotropy strength $K_1 = -5.0 \times 10^3 \text{ J/m}^3$, and damping constant $\alpha = 0.2$. Neg-

ative value of K_1 represents the diagonal directions $\langle 111 \rangle$ in a cubic structure that are at somewhat similar angles as the direction of honeycomb elements with respect to the rectangular coordinate system. During the simulation, the magnetic field is applied along the Y direction, and is incremented by varying step sizes in order to capture the transition states.

The simulated hysteresis curves as a function of magnetic field and associated magnetic profiles for various element sizes are shown in Figs. 1–3. Qualitative differences between the magnetic hysteresis curves for various element size lattices are clearly noticeable. A multitude of magnetic phases tend to emerge near the zero field as the element size changes. The plot of M/M_s vs h , M_s and h being saturation magnetization and magnetic field, respectively, depicts a sharp transition near the zero field in the single domain size element case where the geometrical parameters are smaller than the typical domain size in permalloy, $\sim 18 \text{ nm}$ [19]. The simulated magnetization profile in this state is characterized by the vortex configuration, which is the key element of the spin solid state. In this case, the system exhibits a tendency to attend the spin solid loop state or magnetic charge ordered state or a mixture of both. At moderate thickness and width, t and $w = 10 \text{ nm}$, the density of the magnetic vortex loop decreases. Basically, the magnetic charge profile manifests a disordered configuration. The simulated pattern of the disordered state, consisting of

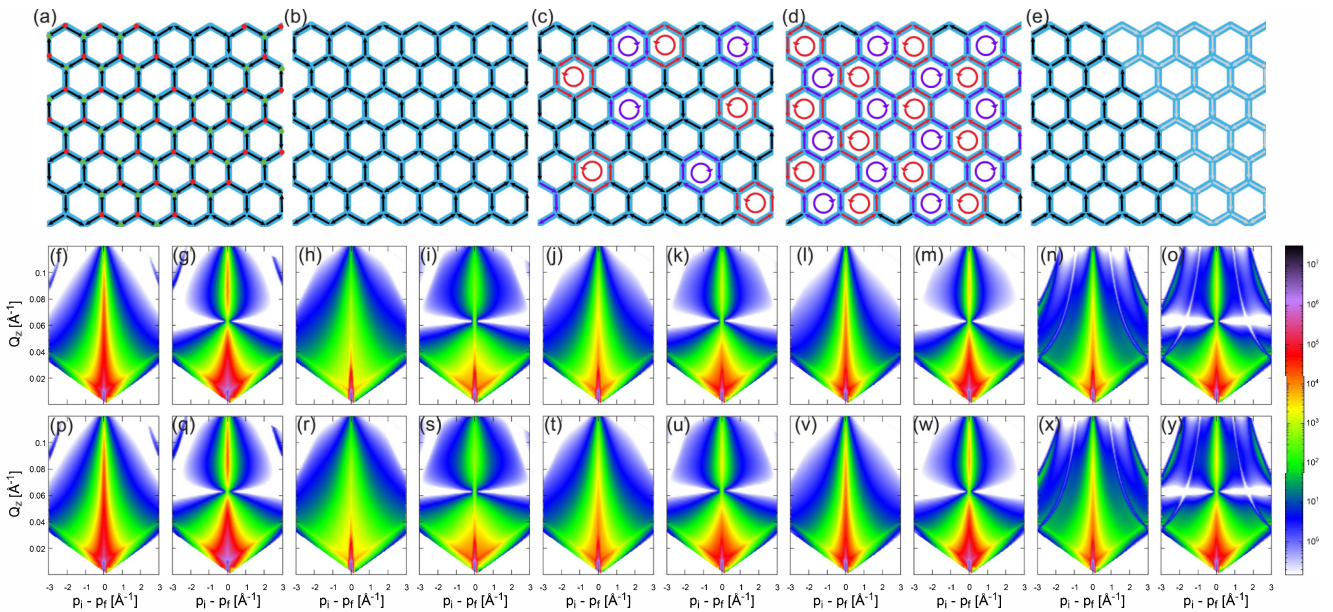


FIG. 5. DWBA simulation of permalloy honeycomb lattice of 50 nm element length. (a)–(e) Top panel—magnetic charge configurations of disordered, spin ice, magnetic charge ordered, spin solid, and low multiplicity magnetic charge stripe states. (f),(g),(p),(q) DWBA simulation of disordered magnetic charge configuration [shown in (a)] in various element size lattices of $50 \text{ nm} \times 5 \text{ nm} \times 5 \text{ nm}$, $50 \text{ nm} \times 5 \text{ nm} \times 10 \text{ nm}$, $50 \text{ nm} \times 10 \text{ nm} \times 5 \text{ nm}$, and $50 \text{ nm} \times 10 \text{ nm} \times 10 \text{ nm}$, respectively. (h),(i),(r),(s) Spin ice configuration [shown in (b)] in various element size lattices of $50 \text{ nm} \times 5 \text{ nm} \times 5 \text{ nm}$, $50 \text{ nm} \times 5 \text{ nm} \times 10 \text{ nm}$, $50 \text{ nm} \times 10 \text{ nm} \times 5 \text{ nm}$, and $50 \text{ nm} \times 10 \text{ nm} \times 10 \text{ nm}$, respectively. (j),(k),(t),(u) Charge ordered configuration [shown in (c)] in $50 \text{ nm} \times 5 \text{ nm} \times 5 \text{ nm}$, $50 \text{ nm} \times 5 \text{ nm} \times 10 \text{ nm}$, $50 \text{ nm} \times 10 \text{ nm} \times 5 \text{ nm}$, and $50 \text{ nm} \times 10 \text{ nm} \times 10 \text{ nm}$, respectively. (l),(m),(v),(w) Spin solid state [shown in (d)] in various element size lattices of $50 \text{ nm} \times 5 \text{ nm} \times 5 \text{ nm}$, $50 \text{ nm} \times 5 \text{ nm} \times 10 \text{ nm}$, $50 \text{ nm} \times 10 \text{ nm} \times 5 \text{ nm}$, and $50 \text{ nm} \times 10 \text{ nm} \times 10 \text{ nm}$, respectively. (n),(o),(x),(y) Stripe state [shown in (e)] in various element size lattices of $50 \text{ nm} \times 5 \text{ nm} \times 5 \text{ nm}$, $50 \text{ nm} \times 5 \text{ nm} \times 10 \text{ nm}$, $50 \text{ nm} \times 10 \text{ nm} \times 5 \text{ nm}$, and $50 \text{ nm} \times 10 \text{ nm} \times 10 \text{ nm}$, respectively.

only $\pm Q$ charges, differs from a recent experimental report where both $\pm Q$ and $\pm 3Q$ charges were found to randomly occupy the honeycomb vertices [17]. The experimental observation was explained in terms of the competing energetics between the nearest neighbor and the next nearest neighbor exchange interactions. Micromagnetic simulations, on the other hand, do not take into account the next nearest neighbor exchange interaction. Perhaps, the inclusion of next nearest exchange interaction is more appropriate in this case, as the interelemental dipolar interaction energy is much smaller, $\sim 15 \text{ K}$. However, the nearest neighbor exchange term is still the most dominant term in the Hamiltonian.

The development of the charge ordered or loop state also seems to occur in the honeycomb lattice with element size of $50 \text{ nm} \times 5 \text{ nm} \times 10 \text{ nm}$; see Fig. 2. The magnetic vortex loops become prevalent as the lattice becomes thinner, $t = 5 \text{ nm}$, tending to develop the spin solid state. Increasing the width and thickness of the honeycomb element seems to drive the vortex loops to the edges of the lattice. An interesting magnetic phase arises in the honeycomb lattice with an element size of $50 \text{ nm} \times 10 \text{ nm} \times 5 \text{ nm}$. MM simulations show that the contiguous bands of $\pm Q$ charges develop. Clearly, this is not a disordered state. Rather, a peculiar type of low multiplicity charge ordering takes place. An entirely different scenario emerges in thin (5 nm) honeycomb lattice with long element, e.g., $100 \text{ nm} \times 10 \text{ nm}$ or $100 \text{ nm} \times 5 \text{ nm}$. Micromagnetic simulation suggests that the system exhibits a well-ordered pattern of $\pm Q$ magnetic charges. As the lattice becomes thicker, the charge ordered vortex loops are formed

across the plaquette. Perhaps, the simulation results can be different for a different set of exchange stiffness and uniaxial anisotropy strength parameters. However, for the same values of A and K_1 , it is inferred that the ratio of the width and the thickness of the honeycomb element play crucial roles in magnetic charge correlation on honeycomb vertices.

Unlike the single domain element size lattice where the honeycomb element behaves as a single magnetic unit, relatively larger element length (50 nm or 100 nm) possibly sets the stage for the dominance of Bloch wall dynamics. So, even though the interelemental dipolar interaction energy is expected to be comparable in a honeycomb lattice of fixed element length, say 50 nm, the remnant magnetization states are drastically different for different w/t ratio. The direct experimental observation of the stripe bands or the disordered state of magnetic charges in a honeycomb lattice with constricted single domain elements can be challenging. It is very difficult to resolve 5–10 nm structure using the MFM technique. A scattering method, such as polarized neutron reflectometry (PNR) or soft x-ray scattering, can be quite suitable for the experimental investigation of micromagnetic phases in these systems. In the case of the PNR method, analysis of the off-specular data using the distorted-wave Born approximation formalism can reveal the underlying magnetic charge configuration. In the following section, we show pertinent DWBA simulations of various magnetic charge states in an artificial magnetic honeycomb lattice. The simulated results can be compared with experimental observations to deduce magnetic charge arrangement in a magnetic honeycomb lattice.

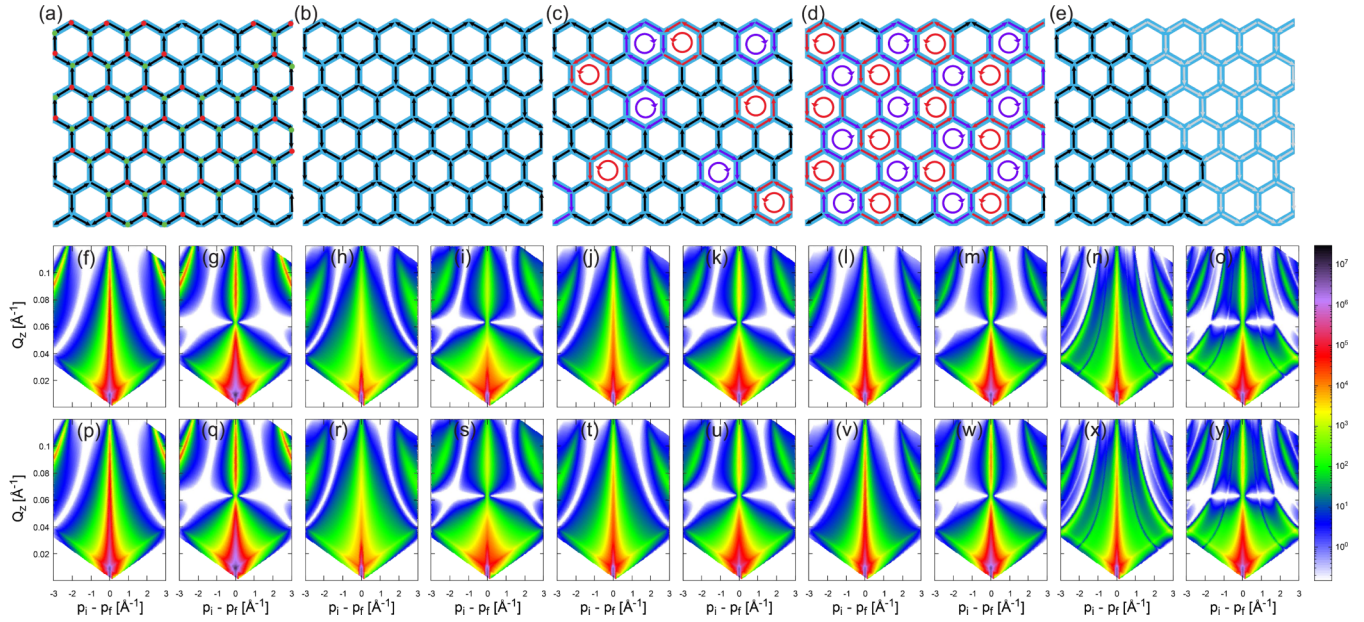


FIG. 6. DWBA simulation of permalloy honeycomb lattice of 100 nm element length. (a)–(e) Top panel—magnetic charge configurations of disordered, spin ice, magnetic charge ordered, spin solid, and low multiplicity magnetic charge stripe states. (f),(g),(p),(q) DWBA simulation of disordered magnetic charge configuration [shown in (a)] in various element size lattices of 100 nm × 5 nm × 5 nm, 100 nm × 5 nm × 10 nm, 100 nm × 10 nm × 5 nm, and 100 nm × 10 nm × 10 nm, respectively. (h),(i),(r),(s) Spin ice configuration [shown in (b)] in various element size lattices of 100 nm × 5 nm × 5 nm, 100 nm × 5 nm × 10 nm, 100 nm × 10 nm × 5 nm, and 100 nm × 10 nm × 10 nm, respectively. (j),(k),(t),(u) Charge ordered configuration [shown in (c)] in 100 nm × 5 nm × 5 nm, 100 nm × 5 nm × 10 nm, 100 nm × 10 nm × 5 nm, and 100 nm × 10 nm × 10 nm, respectively. (l),(m),(v),(w) Spin solid state [shown in (d)] in various element size lattices of 100 nm × 5 nm × 5 nm, 100 nm × 5 nm × 10 nm, 100 nm × 10 nm × 5 nm, and 100 nm × 10 nm × 10 nm, respectively. (n),(o),(x),(y) Stripe state [shown in (e)] in various element size lattices of 100 nm × 5 nm × 5 nm, 100 nm × 5 nm × 10 nm, 100 nm × 10 nm × 5 nm, and 100 nm × 10 nm × 10 nm, respectively.

III. DISTORTED-WAVE BORN APPROXIMATION SIMULATIONS

The distorted-wave Born approximation method relies on the discretization of experimental geometry into the scattering matrix. Basically, we define the honeycomb sample as a multilayer specimen with two layers (**I**) of magnetic film and silicon substrate. The scattering matrix elements for such a system can be described by

$$\langle \psi_i | \delta v | \psi_f \rangle = \sum_{\mathbf{l}} \sum_{\pm i} \sum_{\pm f} \langle \psi_{\mathbf{l}}^{\pm} | \delta v | \psi_{\mathbf{l}}^{\pm} \rangle,$$

where δv is the first order perturbation expansion term of scattering length density [$v(\mathbf{r})$] and ψ_i , ψ_f denotes the incident and final wave functions, respectively. The forward or backward traveling wave function in real space is given by ψ^+ and ψ^- , respectively. While the bottom layer consists of nanostructured silicon with a honeycomb pattern, the top layer is made of permalloy honeycomb lattice. We introduce a layout of the honeycomb pattern of permalloy hexagons with cylinders cut out from the center with a lattice spacing of $a = 31$ nm within the permalloy layer. The form factor for the cylindrical unit is defined as $F = 2\pi R^2 t \text{sinc}(\frac{q_z t}{2}) \exp(i\frac{q_z t}{2}) \frac{J_1(q_{\parallel} R)}{q_{\parallel} R}$, where $q_{\parallel} \equiv \sqrt{q_x^2 + q_y^2}$ and J_1 is a Bessel function of the first kind. The other parameters are radius R and height t that depend on the size of the honeycomb element. The magnetic phases, as inferred from

the micromagnetic simulations, were constructed by using the rectangular elements with fixed magnetization directed along its length. The form factor of the rectangular element is defined by $F = l w t \text{sinc}(\frac{q_x l}{2}) \text{sinc}(\frac{q_y w}{2}) \text{sinc}(\frac{q_z t}{2}) \exp(i\frac{q_z t}{2})$, where l , w , and t denote length, width, and height, respectively. The magnetization elements in the hexagonal lattice develop long-range correlations via the intercluster interference. Correspondingly, the scattering matrix element can be written as

$$\langle \psi_i | \delta v | \psi_f \rangle = \sum_j \exp(i\mathbf{q}_{\parallel} \mathbf{R}_{j\parallel}) \int d^2 r_{\parallel} \exp(i\mathbf{q}_{\parallel} \mathbf{r}_{\parallel}) \times \int dz \phi_i^*(z) F(\mathbf{r} - \mathbf{R}_{j\parallel}; \mathbf{T}_j) \phi_f(z),$$

where $F(\mathbf{r} - \mathbf{R}_{j\parallel}; \mathbf{T}_j)$ is the form factor for the j th element, such that $v_p(\mathbf{r}) = \sum_j F(\mathbf{r} - \mathbf{R}_{j\parallel}; \mathbf{T}_j)$. The elastic scattering cross section is given by $\frac{d\sigma}{d\Omega} = |\langle \psi_i | \delta v | \psi_f \rangle|^2$. To account for the finite-size effect, we have used a 2D lattice interference function with a large isotropic 2D-Cauchy decay function with the lateral structural correlation lengths of $\lambda_{x,y} = 1, 5$, and $10 \mu\text{m}$ for the case of $l = 12, 50$, and 100 nm, respectively. The position correlation is given as $\rho_S G(\mathbf{r}) = \sum_{m,n} \delta(\mathbf{r} - m\mathbf{a} - n\mathbf{b}) - \delta(\mathbf{r})$, with lattice basis (\mathbf{a}, \mathbf{b}). We have also introduced the effects of natural disorder in the system by applying a small Debye-Waller factor corresponding to a position variance of $\langle \mathbf{x} \rangle^2 = 1 \text{ nm}^2$. The interference function

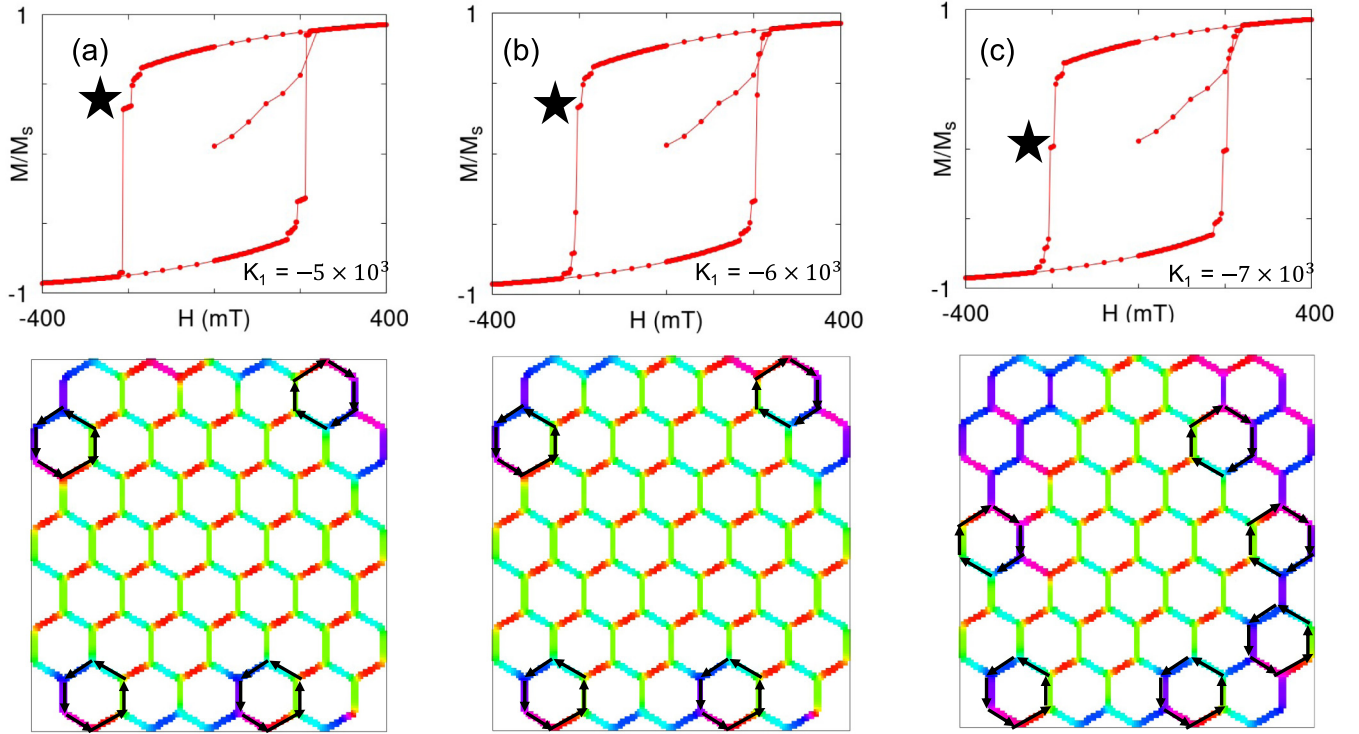


FIG. 7. MM simulation of a representative permalloy honeycomb lattice with element size of $50 \text{ nm} \times 10 \text{ nm} \times 10 \text{ nm}$. Top panel—magnetic hysteresis loop generated for different values of K_1 . Bottom panel—magnetic charge configuration after magnetic transition (marked by asterisk). (a) $K_1 = -5 \times 10^3 \text{ J/m}^3$. (b) $K_1 = -6 \times 10^3 \text{ J/m}^3$. (c) $K_1 = -7 \times 10^3 \text{ J/m}^3$. Varying the anisotropy constant K_1 does not seem to affect the overall charge configuration.

can be written as

$$S(q) = \rho_S \sum_{q_i \in \Lambda^*} \frac{2\pi \lambda_x \lambda_y}{(1 + q_x^2 \lambda_x^2 + q_y^2 \lambda_y^2)^{3/2}}.$$

The simulated off-specular reflectivity profile is generated by using the DWBA modeling, implemented in the BornAgain [28] software [6]. In Figs. 4–6, we show the simulated plots of off-specular reflectivity for various magnetic charge states of spin ice, magnetic charge ordered state, spin solid loop state, disordered state, and the stripe phase in permalloy honeycomb lattice. The spin solid state is modeled by arranging the vortex loops of opposite chirality in an alternating order. In all plots, the y axis represents the out-of-plane scattering vector [$Q_z = \frac{2\pi}{\lambda} (\sin \alpha_i + \sin \alpha_f)$], whereas the difference between the z components of the incident and the outgoing wave vectors [$p_i - p_f = \frac{2\pi}{\lambda} (\sin \alpha_i - \sin \alpha_f)$] is drawn along the x axis. Thus vertical and horizontal directions correspond to the out-of-plane and in-plane correlations, respectively [22]. The specular reflectivity lies along the $x = 0$ line.

As shown in the lower panel of Fig. 4, significant off-specular scattering develops due to the spin-spin correlation in honeycomb lattice of 12 nm element length. The simulated patterns exhibit broad but distinct bands of diffuse scattering along the x axis. In the theoretically predicted spin solid state, the off-specular diffuse scattering is prevalent from $Q_z = 0.06$ to 1 \AA^{-1} . Similar behavior was reported in the PNR measurements on artificial permalloy honeycomb lattice of similar ultrasmall element size ($\sim 12 \text{ nm}$ in length) [6]. Unlike the

spin solid or the magnetic charge ordered states, the off-specular reflection is significantly broader in the case of the disordered phase, consisting of both $\pm Q$ and $\pm 3Q$ magnetic charges. Additionally, the diffuse scattering intensity around the specular line tends to develop the localized pattern along the Z axis with the increasing thickness of the lattice, indicating the onset of finite size correlation. The simulation also reveals the constricted nature of diffuse scattering in both the magnetic charge ordered and the spin solid states in the thicker lattice with 10 nm element length, compared to the thinner lattice. The 10 nm thick lattice with wider elements, $w = 10 \text{ nm}$, exhibits Q_z dependence of diffuse scattering.

DWBA simulation results of 50 nm element size honeycomb lattice, along with the magnetic charge configurations, are shown in Fig. 5. Unlike in the case of 10 nm element size honeycomb, the diffuse scattering tends to shrink along the Q_z direction in this case. Also, the qualitative difference between the reflectometry profiles for the spin ice and the spin solid phases becomes weaker as the lattice becomes thinner (5 nm thickness). In 10 nm thick lattice, there is an observable distinction between the three magnetic phases of spin ice, charge ordered state, and the spin solid state. However, once again, the disordered phase manifests stronger diffuse scattering, compared to the theoretically predicted states. Micromagnetic simulations revealed that a 50 nm element size honeycomb lattice tends to develop contiguous bands of $\pm Q$ magnetic charges, resembling a stripelike pattern, in thinner lattice. Simulated reflectometry profiles for this state for different lattice thicknesses are shown in Figs. 5(e) and 5(i).

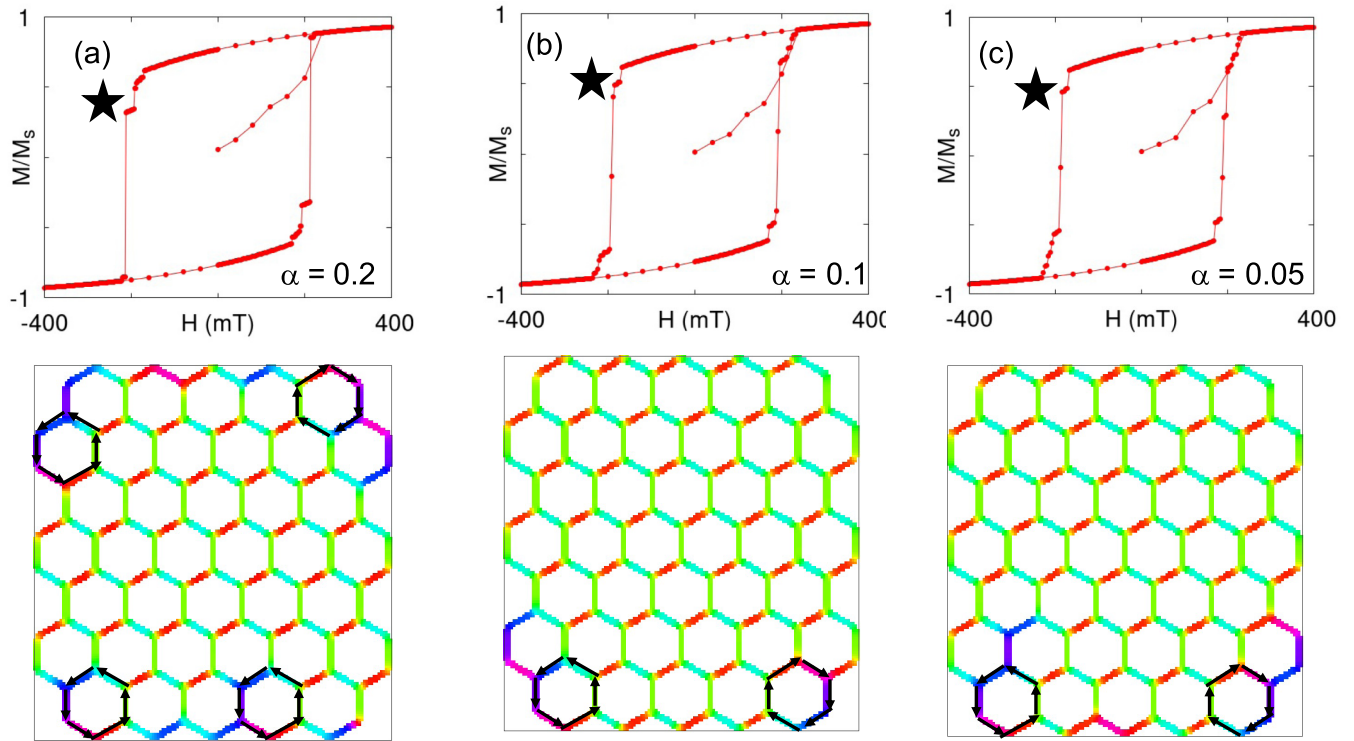


FIG. 8. MM simulation of a representative permalloy honeycomb lattice with element size of $50 \text{ nm} \times 10 \text{ nm} \times 10 \text{ nm}$. Top panel—magnetic hysteresis loop generated for different values of α . Bottom panel—magnetic charge configuration after magnetic transition (marked by asterisk). (a) $\alpha = 0.2$. (b) $\alpha = 0.1$. (c) $\alpha = 0.05$. Varying the damping constant α does not seem to affect the overall charge configuration.

In this case, we observe the patches of distinct diffuse scattering along the x axis, indicating q -dependent in-plane correlation. As the honeycomb element becomes wider, $w = 10 \text{ nm}$, the diffuse scattering assumes a more conical shape. Finally, we show the DWBA simulated plots of 100 nm element length honeycomb lattice in Fig. 6. The width and thickness of the honeycomb element are kept in the single domain limit. Therefore, a honeycomb element is multidomain along the length, but exhibits the single domain characteristic along width and thickness directions. We observe strong qualitative difference between the simulated profiles for thin (5 nm) and thick (10 nm) lattices. However, the distinction between the theoretically predicted phases of spin ice and spin solid or the disordered state is apparently very weak for a given thickness of the lattice. Also, numerical results do not seem to be much affected by a variation in width of the honeycomb element (from 5 nm to 10 nm). Perhaps, the simulated reflectometry profiles can exhibit distinct patterns for larger thicknesses or broader elements of the lattice. We have not explored the multidomain structure of honeycomb elements in all three directions. In the latter case, domain wall motion along different directions makes the micromagnetic simulation analysis more cumbersome.

IV. DISCUSSION

Artificial magnetic honeycomb lattice is known to exhibit a plethora of theoretically predicted emergent phases as functions of temperature and magnetic field [1]. In this article, we have presented numerical simulation results on a honeycomb

lattice made of permalloy ($\text{Ni}_{0.81}\text{Fe}_{0.19}$) elements with varying geometrical sizes. Large shape anisotropy in permalloy makes it feasible to create two-dimensional geometrically frustrated lattice structures that are the subject of intense experimental investigations presently. Additionally, the uniaxial anisotropy, K_1 term, ensures that the magnetic moment is aligned along the length of the connecting element. Micromagnetic simulations on honeycomb lattice of relatively smaller element sizes reveal additional magnetic phases of disordered charge configuration and contiguous bands of $\pm Q$ charges (termed as stripe-type phase) in the remnant state. While the disordered state consists of a random distribution of $\pm Q$ and $\pm 3Q$ charges, the stripe phase is characterized by the coexisting bands of ordered patterns of $+Q$ and $-Q$ charges. Experimental confirmation to a disordered ground state was recently reported in permalloy honeycomb lattice of single domain size element [17]. A disordered ground state in honeycomb lattice is theoretically argued to arise at low temperature where the next nearest neighbor exchange interaction, J_2 , can play an important role [14]. Despite the absence of the J_2 term in the Hamiltonian in the OOMMF platform, our MM simulation predicts the development of a disordered ground state in honeycomb lattice. It suggests that the nearest exchange term, J_1 , is the most dominant term. Magnetic charges manifest highly dynamic behavior to the lowest measurement temperature in the disordered phase [16]. Experimental observation of the stripe-type phase of low multiplicity magnetic charges can be very exciting.

The occurrence of magnetic phases in honeycomb lattice is determined by the energetic interplay of four energy terms:

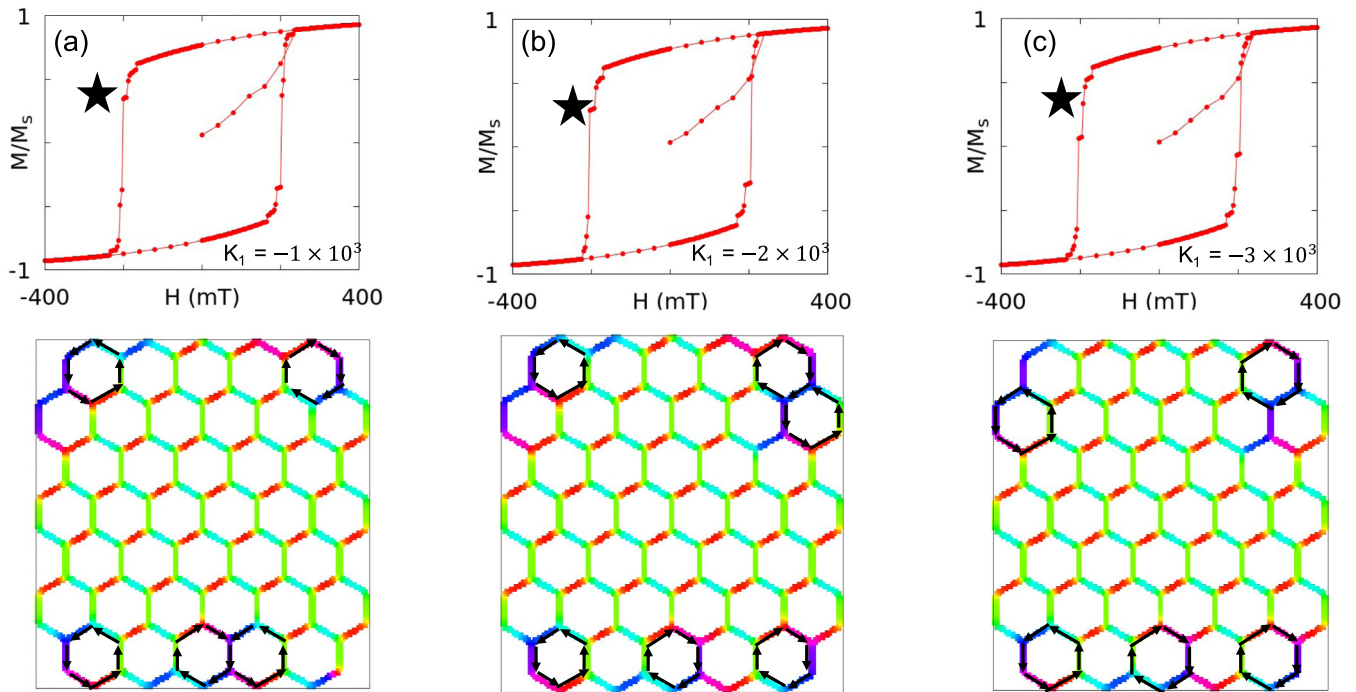


FIG. 9. MM simulation of a representative permalloy honeycomb lattice with element size of $50 \text{ nm} \times 10 \text{ nm} \times 10 \text{ nm}$ for lower values of K_1 . Top panel—magnetic hysteresis loop generated for different values of K_1 . Bottom panel—magnetic charge configuration after magnetic transition (marked by asterisk). (a) $K_1 = -1 \times 10^3 \text{ J/m}^3$. (b) $K_1 = -2 \times 10^3 \text{ J/m}^3$. (c) $K_1 = -3 \times 10^3 \text{ J/m}^3$. Varying the anisotropy constant K_1 to lower values does not seem to affect the overall charge configuration.

exchange interaction, demagnetization energy, magnetostatic (dipolar) energy, and Zeeman energy. The emergence of the spin ice state, as depicted in the 100 nm element size lattice, is dominated by the dipolar interaction. Large element size is accompanied by large magnetic moment, which makes the dipolar interaction a significant term in the Hamiltonian. Spin solid order and the stripe phase, on the other hand, are dominated by the exchange interaction, as manifested by the ultrasmall (15 nm length) and the small (50 nm length) element size lattices, respectively, in MM simulations. Additionally, smaller element size has relatively smaller demagnetization factor, which facilitates the magnetic transition process near zero field with negligible Zeeman energy. The energetics involving dipolar and exchange energies depend on the size of the honeycomb lattice elements. Thus micromagnetic simulation results provide a comparative overview of magnetic phase development in the artificial permalloy honeycomb lattice system.

Experimental investigation of magnetic states in artificial honeycomb lattice, made of single domain size magnetic elements, is a challenging task. Unlike the case of the large element size magnetic honeycomb where the magnetic force microscopy (MFM) has proved to be an effective probe, the direct imaging of magnetic charges in such a small geometry is not feasible. The spatial resolution ($\sim 50 \text{ nm}$) of MFM is larger than the geometrical dimension of an individual element in the single domain limit. The scattering method, such as PNR, provides an appropriate platform to the experimental quest. The neutron reflectometry method, as available on MagRef instrument on BL-4A beam line at the Spallation Neutron Source at the Oak Ridge National Laboratory, is a versatile probe to

study magnetic charge correlation in artificial magnetic lattice of single domain size elements. While the specular reflection provides information about the underlying magnetism and the magnetic layer thickness, the off-specular data can be used to infer the nature of planar correlation of magnetic charges in the lattice. However, modeling of the off-specular data is not trivial. The DWBA method is a commonly used numerical technique to extract the intended information. The simulation results, presented in this article, are expected to provide a useful guide in this pursuit. Further theoretical research on understanding the development of a stripe charge ordered phase in artificial magnetic honeycomb lattice is highly desirable.

ACKNOWLEDGMENT

Research at the University of Missouri is supported by the U.S. Department of Energy, Office of Basic Energy Sciences under Grant No. DE-SC0014461.

APPENDIX

We have performed additional micromagnetic simulations to test the validity of the results for small variation in intrinsic parameters, e.g., the uniaxial anisotropy constant K_1 and the damping constant α . As shown in Figs. 7 and 8, modest variation up to 20% or 30% (limit of validity) in the value of K_1 does not seem to affect the overall outcome. For instance, the development of vortex loop states at the boundary for $K_1 = -5 \times 10^3 \text{ J/m}^3$ is reproducible at $K_1 = -6 \times 10^3 \text{ J/m}^3$ or $K_1 = -7 \times 10^3 \text{ J/m}^3$. Reducing the anisotropy constant K_1 does not seem to affect the overall outcome either; see Fig. 9.

Similarly, a small variation in the damping constant does not affect the magnetic transition process, as shown in Fig. 8. Thus

our simulation results are robust against modest variation in intrinsic parameter values.

-
- [1] S. Skjaerervo, C. Marrows, R. Stamps, and L. Heyderman, *Nat. Rev. Phys.* **2**, 13 (2020).
- [2] P. Schiffer and C. Nisoli, *Appl. Phys. Lett.* **118**, 110501 (2021).
- [3] B. Summers, A. Dahal, and D. K. Singh, *Adv. Electron. Mater.* **4**, 1700500 (2018).
- [4] C. Castelnovo, R. Moessner, and S. Sondhi, *Nature (London)* **451**, 42 (2008).
- [5] G. Chern and O. Tchernyshyov, *Phil. Trans. Royal Soc. A* **370**, 5718 (2012).
- [6] A. Glavic, B. Summers, A. Dahal, J. Kline, W. Van Herck, and A. Sukhov, A. Ernst, and D. K. Singh, *Adv. Sci.* **5**, 1700856 (2018).
- [7] O. Sendetskyi, L. Anghinolfi, V. Scagnoli, G. Moller, N. Leo, A. Alberca, J. Kohlbrecher, J. Luning, U. Staub, and L. Heyderman, *Phys. Rev. B* **93**, 224413 (2016).
- [8] C. Paulsen, S. R. Giblin, E. Lhotel, D. Prabhakaran, G. Balakrishnan, K. Matsuhira, and S. T. Bramwell, *Nat. Phys.* **12**, 661 (2016).
- [9] Y. Shen, O. Petrova, P. Mellado, S. Daunheimer, J. Cumings, and O. Tchernyshyov, *New J. Phys.* **14**, 035022 (2012).
- [10] B. Summers, L. Debeer-Schmitt, A. Dahal, A. Glavic, P. Kampschroeder, J. Gunasekera, and D. K. Singh, *Phys. Rev. B* **97**, 014401 (2018).
- [11] V. Schanilec, B. Canals, V. Uhlir, L. Flajsman, J. Sadilek, T. Sikola, and N. Rougemaille, *Phys. Rev. Lett.* **125**, 057203 (2020).
- [12] A. Farhan, M. Saccone, C. Peterson, S. Dhuey, R. Chopdekar, Y. Huang, N. Kent, Z. Chen, M. Alava, T. Lippert, A. Scholl, and S. van Dijken, *Sci. Adv.* **5**, eaav6380 (2019).
- [13] A. Frotanpoura, J. Woods, B. Farmer, A. Kaphle, and L. De Long, *Appl. Phys. Lett.* **118**, 042410 (2020).
- [14] A. S. Wills, R. Ballou, and C. Lacroix, *Phys. Rev. B* **66**, 144407 (2002).
- [15] R. Siddharthan, B. Shastry, A. Ramirez, A. Hayashi, R. Cava, and S. Rosenkranz, *Phys. Rev. Lett.* **83**, 1854 (1999).
- [16] Y. Chen, G. Yumnam, J. Guo, L. Stingaciu, P. Zolnierczuk, V. Lauter, and D. K. Singh, *iScience* **24**, 102206 (2021).
- [17] G. Yumnam, Y. Chen, J. Guo, V. Lauter, K. Jiang, and D. K. Singh, *Adv. Sci.* **11**, 2004103 (2021).
- [18] Y. Chen, B. Summers, A. Dahal, V. Lauter, G. Vignale, and D. K. Singh, *Adv. Mater.* **31**, 1808298 (2019).
- [19] J. M. D. Coey, *Spin Electronics* (Springer, New York, 2000), Chap. 12.
- [20] A. Dahal, Y. Chen, B. Summers, and D. K. Singh, *Phys. Rev. B* **97**, 214420 (2018).
- [21] S. K. Sinha, E. B. Sirota, S. Garoff, and H. B. Stanley, *Phys. Rev. B* **38**, 2297 (1988).
- [22] V. Lauter, H. Lauter, A. Glavic, and B. Toperverg, *Reference Module in Materials Science and Materials Engineering* (Elsevier, Amsterdam, 2016), pp. 1–27.
- [23] M. J. Donahue and D. G. Porter, OOMMF User's Guide, Version 1.0, Interagency Report No. NISTIR 6376, National Institute of Standards and Technology, Gaithersburg, MD, 1999 (unpublished).
- [24] D. K. Singh, R. Krotkov, and M. T. Tuominen, *Phys. Rev. B* **79**, 184409 (2009).
- [25] L. D. Landau and E. M. Lifshitz, *Phys. Z. Sowjetunion* **8**, 153 (1935).
- [26] T. L. Gilbert, *IEEE Trans. Magn.* **40**, 3443 (2004).
- [27] W. F. Brown, *Micromagnetics* (Wiley, New York, 1963).
- [28] BornAgain—Software for simulating and fitting x-ray and neutron small-angle scattering at grazing incidence, <http://www.bornagainproject.org>, version 1.7.1.